

An Extended Study of Gear-Ratio-Aware Standard Cell Layout Generation for DTCO Exploration

Chung-Kuan Cheng, *Fellow, IEEE*, Andrew B. Kahng, *Fellow, IEEE*, Bill Lin, *Senior Member, IEEE*, Yucheng Wang, *Graduate Student Member, IEEE*, and Dooseok Yoon, *Graduate Student Member, IEEE*

Abstract—Advanced nodes decouple contacted poly pitch (CPP) and lower-metal pitch to improve routability. We present CPCell, an efficient standard-cell layout generation framework, to support arbitrary gear ratio (GR) and offset parameters through a fine-grained layered grid graph and constraint-programming-based placement–routing co-optimization. Layout quality is improved via Middle-of-Line routing, M0 pin enablement, pin accessibility constraints and a weighted multi-objective formulation that jointly optimizes cell layouts. To scale to netlists with up to 48 transistors, we incorporate acceleration techniques including transistor clustering, identical transistor partitioning, routing lower bound tightening and early termination strategies. Comprehensive cell-level and block-level studies are conducted to evaluate GR and offset choices, quantify the benefits of the proposed objectives and assess their impact on power, performance, area and IR-drop outcomes.

I. INTRODUCTION

Early nodes assumed uniform scaling between contacted poly pitch (CPP) and metal pitch. Advanced nodes decouple CPP and lower-metal pitch to reduce routing congestion on lower metals [21]. As metal pitch scales faster than CPP [35], the CPP-to-metal-1 (M1) pitch ratio, called *gear ratio* (GR), becomes a key design-technology co-optimization (DTCO) parameter [8]. GR affects cell-level routability and block-level implementation quality. Reducing the M1 pitch increases the number of M1 tracks and reduces routing congestion. An *offset* is a parameter complementary to GR that specifies the distance between the leftmost poly column and the leftmost M1 column. Introducing an offset on the M1 grid shifts the column alignment to ensure compatibility between the local cell grid and the global (chip) routing grid, thereby enabling placement legalization under complex gear ratio settings.

Figure 1 illustrates three representative GR settings and their M1 routing resources within a 7-CPP cell width. Figure 1(a) shows that the conventional 1:1 GR [20] yields six usable M1 columns. As the M1 pitch decreases, routing resources increase. A 3:2 GR yields 10 M1 columns (Figure 1(b)). A 5:3 GR yields 11 columns without offset and up to 12 columns with an offset (Figure 1(c)). Offset variants are needed because non-1:1 GRs can misalign the poly and M1 grids [6]. Offset restores grid alignment and prevents block-level legalization failures, leading to more accurate evaluation data used to inform technology decisions.

Prior work studies gear ratio and offset, mainly using post-processed layouts or backside power delivery. Jeong et al. [14] propose a non-1:1 gear-ratio-aware DTCO framework that improves pin accessibility using post-placement pin relocation and post-routing stretching. Their method reduces routing

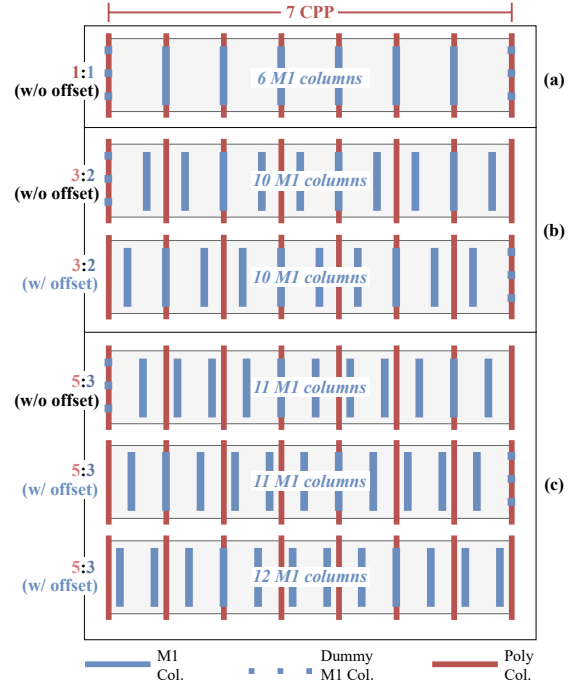


Fig. 1. An example of M1 routing resources corresponding to different gear-ratio settings within a 7-CPP cell layout. Dummy M1 columns are used at the left-end and the right-end of the cell layout to avoid overlapping columns with adjacent cell layouts. The rest of the M1 columns are counted as available routing resources. (a) 1:1 GR. (b) 3:2 GR with its offset variant. (c) 5:3 GR with its two offset variants.

violations without increasing wirelength, timing or power. However, because it introduces gear ratio effects as post-processing, it does not model non-1:1 GR effects during cell generation. Cheng et al. [7] integrate non-1:1 gear ratios into SMT-based standard cell generation with backside power delivery, but they evaluate only area. Comprehensive studies in sub-7 nm technology options [9] that jointly evaluate GR and offset choices on both cell-level and block-level metrics are still limited.

In this work, we extend the prior study [6] by introducing CPCell with the following items.

- (1) *CPCell Framework*: CPCell is a standard-cell layout generation tool and a continuation of the prior SP&R framework [20] and various other prior works [4] [3] [18] with the emphasis on customization and block-level power, performance and area (PPA). It is compatible with CP-SAT solver from OR-Tools [39], which employs an integer- and SAT-based encoding compatible with previous SMT formulations in Z3 [34]. The workflow of

CPCell is depicted in Figure 2. Table I summarizes the design-technology co-optimization (DTCO) capabilities of representative standard-cell layout generation frameworks. Compared to prior SMT-, MILP- and heuristic-based approaches, CPCell is the only framework that simultaneously supports arbitrary gear ratios and offset variants while guaranteeing global optimality across placement and routing objectives under PROBE3.0 Process Design Kit (PDK) [9].

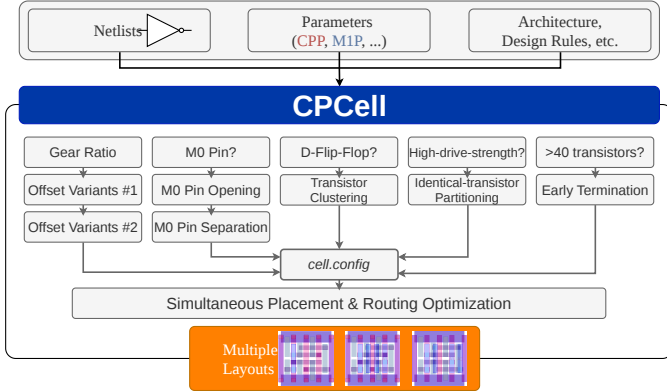


Fig. 2. Proposed CPCell workflow. The inputs include the cell netlist, design rules and gear ratio settings. For each cell, CPCell generates a configuration file that encodes offset variants (based on gear ratio), M0 pin settings and acceleration settings. All offset variants are enumerated and multiple layout candidates are generated per cell.

- (2) *Gear Ratio & Offset*: CPCell supports flexible metal pitch and offset parameters. These settings modulate routing resources and impact metrics at both the cell and block-level (see Section VI and Section VII). Prior work [6] explores 3:2 and 5:3 GR but omits offset variants, leading to placement legalization issues that limit the achievable PPA. Figure 3(a) shows the placement condition under 3:2 GR (from Figure 1(b)). The local poly and M1 grids must align with the global grids. Otherwise, the cell violates the routing grid as shown in Figure 3(b) for a 2-CPP cell under 3:2 gear ratio. To fix this, the local M1 grid uses an offset to align with the global grids (see Figure 3(c)). Consequently, designers must enumerate offset options for each cell netlist to cover all legal grid alignments. CPCell streamlines this process by generating multiple layouts with these offset options.
- (3) *Layout enhancement*: Prior work relies primarily on M1 for vertical routing [6] [9]. This reliance creates routing blockages and reduces block-level routability. We add Middle-of-Line (MOL) routing for intra-cell connectivity [32] [15] and enable M0 pins to improve block-level access. Figure 4 compares DFFHQX1 layouts under a 3:2 GR. CPCell reduces cell width by four CPP and enables M0 pins without adding M1 routing.
- (4) *Acceleration Techniques*: Gear ratio and offset parameters introduce additional complexity for routing as mentioned in prior work [6]. For example, D flip-flops require user-given partitioning. We design a set of complementary

acceleration techniques that are tailored to both the structure of transistor-level netlists and the underlying CP-SAT solving behavior. *Transistor clustering* exploits structural regularities among the transistors by identifying clusters. *Identical transistor partitioning* (ITP) eliminates ordering redundancy. *Routing lower bound tightening* (RLBT) accelerates optimality certification by tightening the lower bound early in the search. *Early termination with a relative optimality gap* enables scalable optimization for large netlists by providing a principled trade-off between runtime and optimality. Experiments show that our acceleration methods reduce runtime by up to 88.96% and scale to netlists with up to 48 transistors.

Section II introduces the proposed graph-based framework for constraint formulation. Section III presents the objective functions. Section IV introduces M0 pin accessibility constraints. Section V describes the acceleration techniques used to reduce solver runtime. Section VI evaluates the impact of gear ratio and offset at cell-level using various layout metrics. Section VII assesses block-level implications in terms of PPA and IR-drop. Our code, cell layout, Liberty, and evaluation scripts are open source and available on GitHub [42].

II. CONSTRAINT FORMULATION

Recall that *gear ratio* (GR) is the ratio between (contacted) poly and M1 pitches. Common GR values include integer or half-integer ratios, such as 1:1 or 3:2.

Given any GR parameter, our tool dynamically formulates constraints based on a graph structure. In terms of constraint formulation, we incorporate largely the same set of constraints as SP&R [20]. The novelty of our framework lies in its fine-grained graph structure that permits the capture of all the gear ratio details, which are essential for the constraint formulation. Our framework treats pitches as variables to construct a relative layered grid graph, representing a potential cell layout.

In our graph structure, we consider a four-layer design¹: placement layer L^1 (vertical), M0 layer L^2 (horizontal), M1 layer L^3 (vertical), and M2 layer L^4 (horizontal). Since our formulation relies on vertex-based constraints, accurately capturing the varying distances between vertices is crucial for satisfying complex design rules [33].

A. Relative Layered Grid Graph Construction

Before graph construction, we determine the total cell width and the layer-specific column and row sets. The total cell width w_{total} is the horizontal boundary of the layout. It is derived from the allowable diffusion break counts (c_{db}), the contacted poly pitch (mp^1), and the maximum of the accumulated PMOS (w_p) and NMOS (w_n) transistor widths:

$$w_{\text{total}} = \max(w_p, w_n) + c_{db} \cdot mp^1, w_p \in \mathbb{Z}^+, w_n \in \mathbb{Z}^+. \quad (1)$$

Let i be the index of the layers. We discretize the layout area into a grid of valid coordinate points. These points

¹While this work utilizes a four-layer stack consistent with the target PDK, our proposed framework generalizes to arbitrary layer counts, subject to increased computational complexity.

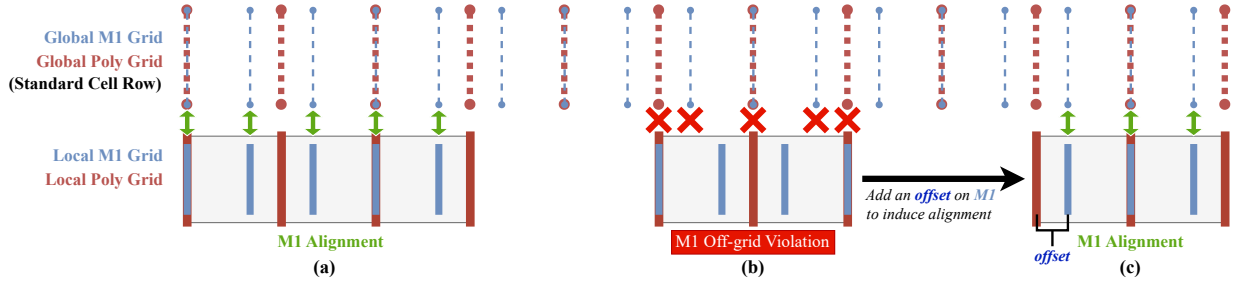


Fig. 3. Three placement scenarios for 3:2 GR cell layouts. (a) A 3-CPP cell layout can be legally placed onto the standard-cell row due to alignment between the local and the global grids. (b) Due to misalignment, a 2-CPP cell layout cannot be legally placed onto the grid. To legalize the placement, either the cell must be relocated—burdening the routing process—or a cell layout with an offset on M1 can be created. (c) In the same scenario as (b), the 2-CPP cell can be legally placed onto the grid with an offset on M1 to induce alignment between the local and the global grids.

TABLE I
SUMMARY OF AVAILABLE DTCO FEATURES IN STANDARD-CELL LAYOUT GENERATION TOOLS.

Framework	SP&R [20]	PROBE3.0 [9]	Csyn-fp [1]	NVCell [28] [12]	SMTCell-GR [6]	SO3 [5]	Au-Medal [15]	Our Work (CPCell)
Arbitrary Gear Ratio	No	No	No	No	Yes	No	No	Yes
Arbitrary Offset	No	No	No	No	No	No	No	Yes
Method	SMT	SMT	Tree Search, DP, SMT, MILP	SA, RL, GA	SMT	MILP	SMT	CP
Optimality Condition	Δ (Prioritized)	Δ (Prioritized)	Δ (Sequential)	Δ (Sequential)	Δ (Prioritized)	Yes	Δ (Routing)	Yes
MOL Routing	No	No	Yes	Unspecified	No	Yes	Yes	Yes
Parameterizable Gate Cut	No	No	No	No	No	No	No	Yes
Acceleration Technique	<ul style="list-style-type: none"> Symmetry breaking Datapath-aware partitioning 	<ul style="list-style-type: none"> Symmetry breaking Datapath-aware partitioning 	<ul style="list-style-type: none"> Diffusion-based clustering Redundant branch pruning Fast cost estimation 	<ul style="list-style-type: none"> ML-based clustering 	<ul style="list-style-type: none"> Symmetry breaking Datapath-aware partitioning 	<ul style="list-style-type: none"> Symmetry breaking Maximum occupying track Misaligned gate specification Structure-driven partitioning 	Δ (Routing)	<ul style="list-style-type: none"> Symmetry breaking Transistor clustering ITP RLBT Early termination
Technology	PROBE	PROBE	ASAP7 [32]	Unspecified	PROBE	PROBE	ASAP7 [32]	PROBE

SMT: Satisfiability modulo theories; DP: Dynamic Programming; SA: Simulated Annealing; RL: Reinforcement Learning; GA: Genetic Algorithm; MILP: Mixed Integer Linear Programming; CP: Constraint Programming; ITP: Identical Transistor Partitioning; RLBT: Routing Lower Bound Tightening. Key additions are highlighted in **Bold**.

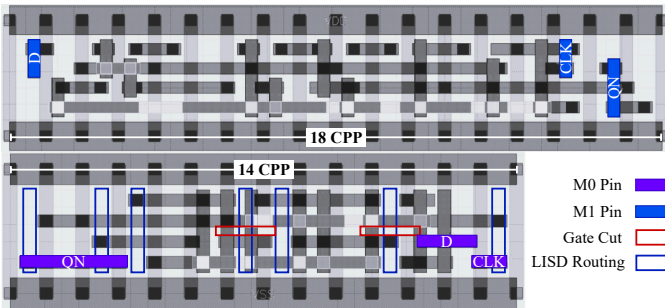


Fig. 4. Comparison of DFFHQ_N_X1 layouts generated by PROBE3.0 [9] (top) and CPCell (bottom) under 3:2 GR. CPCell achieves 4-CPP reduction with gate cuts and enables M0 pins without M1 routing.

correspond to the intersections of physical routing tracks. Let C^i and R^i denote the set of valid x-coordinates (columns) and y-coordinates (rows), respectively, for each layer L^i . Our targeted cell layout is unidirectional, meaning that each layer has tracks running in a direction orthogonal to that of its

neighbor layer(s), with mp^i as the pitch between adjacent tracks. Therefore, a horizontal layer shares columns with its adjacent vertical layer(s); a vertical layer shares rows with its adjacent horizontal layer(s). Since gear ratio is only defined between vertical layers, horizontal layers must have the same pitch (i.e., $mp^2 = mp^4$) and thus all layers must share the same set of rows,

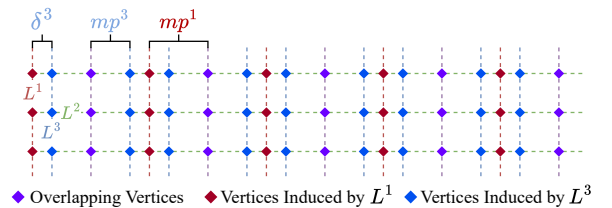


Fig. 5. Top-down view of the irregular pattern of columns on L^2 induced by different pitch values on L^1 and L^3 .

$$R^1 = R^2 = R^3 = R^4 = \{h \cdot mp^i \mid h \in \mathbb{Z}^+, h \leq t\}, \quad (2)$$

$$i = 2 \text{ or } 4.$$

TABLE II
SUMMARY OF SYMBOLS AND DESCRIPTIONS.

Symbol	Description
$G = (\mathcal{V}, \mathcal{E})$	The relative layered grid graph consisting of disjoint vertex sets \mathcal{V} and edge sets \mathcal{E} .
$v = (i; r; c)$	A vertex triplet representing a specific coordinate defined by layer i , row r and column c .
L^i	The i^{th} layer of the design.
$w_{total}, w_p, w_n, c_{db}$	The total cell width, PMOS transistor width, NMOS transistor width and the allowable diffusion break count, respectively.
mp^i	The pitch value between adjacent tracks on layer L^i .
δ^i	The offset value from the left edge for layers L^i .
C^i	The column set for layer L^i .
R^i	The row set for layer L^i .
scx_c	The super cut node on column c used to abstract the shape and flow of cut rows.
$g(v, \{L, R, F, B\})$	Geometric variables (GVs) assigned to vertex v indicating the End-of-Line of a metal segment in direction left, right, front and back.
P	The set of external pins.
\mathcal{N}	The set of nets excluding power and ground nets.
s_n	The source vertex of net n .
T_n	The set of terminal vertices of net n .
$t_{n,k}$	The k^{th} terminal (sink) vertex of net n .
$f_{n,k}(a)$	A binary flow variable indicating whether the routing path from s_n to terminal $t_{n,k}$ uses arc $a_{(u,v)}$.
\mathcal{A}	The set of directed arcs obtained by orienting each undirected edge in \mathcal{E} in both directions.
$\mathcal{A}^+(v), \mathcal{A}^-(v)$	The set of outgoing arcs from vertex v and the set of incoming arcs to vertex v , respectively.
$a_{(u,v)}$	A directed routing arc from vertex u to vertex v .

Algorithm 1: Column Set Creation

```

1 for  $i \in \{1, 3\}$  do
2    $c \leftarrow \delta^i$ 
3    $C^i \leftarrow \emptyset$ 
4   while  $c \leq w_{total}$  do
5      $C^i \leftarrow C^i \cup \{c\}$ 
6      $c \leftarrow c + mp^i$ 
7    $C \leftarrow C \cup C^i$ 
8 for  $i \in \{2, 4\}$  do
9    $C^i \leftarrow C^{i-1} \cup C^{i+1}$  // Implicitly,  $C^5 = \emptyset$ 
10   $C \leftarrow C \cup C^i$ 
11 return  $C$ 

```

Creating the column sets C^i must allow for $mp^1 \neq mp^3$ and must consider offsets δ . Figure 5 illustrates how the mp^1 and mp^3 values can result in an irregular pattern of columns on L^2 . The column set C^2 must contain all columns from both C^1 and C^3 to represent the densely placed routing tracks, with overlapped columns being merged to avoid redundancy. We achieve this using Algorithm 1, which iteratively creates columns for vertical layers first (Lines 1–7) and then merges them on horizontal layers without repetition (Lines 8–10), ensuring uniqueness for each column in a horizontal layer.

After creating C and \mathcal{R} , we construct a *relative layered grid graph* $G = (\mathcal{V}, \mathcal{E})$, where \mathcal{V} and \mathcal{E} are a set of disjoint vertex sets and a set of disjoint edge sets, respectively:

$$\mathcal{V} = \{V^i | i \in \{1, \dots, 4\}, \quad (3)$$

$$V^i = \{v | v = (i; r; c), r \in R^i, c \in C^i\} \quad (4)$$

$$\mathcal{E} = \{E^i | i \in \{1, \dots, 4\}, \quad (5)$$

$$E^i = \{e | e = (v_1, v_2), v_1 \in V^i, v_2 \in V^j, j \in \{i-1, i\}\}. \quad (6)$$

Algorithm 2: Relative Layered Grid Graph Construction

```

1 for  $i \in \{1..4\}$  do
2    $V^i \leftarrow \emptyset, E^i \leftarrow \emptyset$ 
3   // In the order of increasing rows and columns
4   for  $r \in R^i$  do
5     for  $c \in C^i$  do
6        $v \leftarrow (i; r; c)$ 
7        $V^i \leftarrow V^i \cup \{v\}$ 
8       if layer  $i$  is horizontal then
9         Get the nearest left vertex  $v_a$  in  $V^i$ 
10         $E^i \leftarrow E^i \cup \{(v, v_a)\}$ 
11      if layer  $i$  is vertical then
12        Get the nearest lower vertex  $v_b$  in  $V^i$ 
13         $E^i \leftarrow E^i \cup \{(v, v_b)\}$ 
14      // if via can be constructed below
15       $v_c \leftarrow (i-1; r; c)$ 
16      if  $v_c \in V^{i-1}$  then
17         $E^i \leftarrow E^i \cup \{(v, v_c)\}$ 
18   $\mathcal{V} \in V^i, \mathcal{E} \in E^i$ 
19 return  $\mathcal{V}, \mathcal{E}$ 

```

Each vertex v is a triplet $(i; r; c)$ that contains layer i , row r and column c . Each edge e is a pair of vertices whose locations are adjacent (i.e., nearest neighbors) created along the direction of this layer. To generate \mathcal{V} and \mathcal{E} , we use Algorithm 2: for horizontal layers, edges are created along each row (Lines 8–10); for vertical layers, edges are created along each column (Lines 11–13). These edges facilitate intra-layer routing. Edges between layers, called vias, are created if and only if the two vertices are on adjacent layers and have the same *row* and *column* (Lines 14–17).

B. Routing

We model the routing task as a *multi-commodity flow* problem [10] [13] on the relative layered grid graph as illustrated in Figure 6. CPCell employs a directed routing encoding, which we empirically find to scale better than prior undirected models [6] [18]. Each edge $\{u, v\} \in E$ is represented by two directed arcs $a_{(u,v)}, a_{(v,u)} \in \mathcal{A}$, where \mathcal{A} denotes the set of directed arcs. Routing flow is defined exclusively on these arcs to control direction and flow capacity.

Middle-of-Line (MOL) Routing. MOL routing [32] uses the Local Interconnect Source-Drain (LISD) and gate layers to connect adjacent terminals without consuming (global) metal routing resources. When terminals align in a column, they can be “merged” through the shared active region. This allows routing to treat the column as a single sink, rather than requiring distinct flows for every terminal.

Let \mathcal{N} denote the set of signal nets. For each net $n \in \mathcal{N}$, let s_n be the source and $T_n = \{t_{n,0}, \dots, t_{n,K_n-1}\}$ be the set of sink terminals. We model global routing using binary flow variables:

$$f_{n,k}(a) \in \{0, 1\}, \quad \forall a \in \mathcal{A}, \quad (7)$$

indicating whether the path from s_n to terminal $t_{n,k}$ traverses arc a . To capture the interaction between global routing flow and local MOL connectivity, we introduce *super cut node*, $scx_c \in \{0, 1\}$, which determines the physical continuity of the placement grid (L^1) at column c . $scx_c = 1$ represents a physical break—either as a gate cut at even columns or a LISD

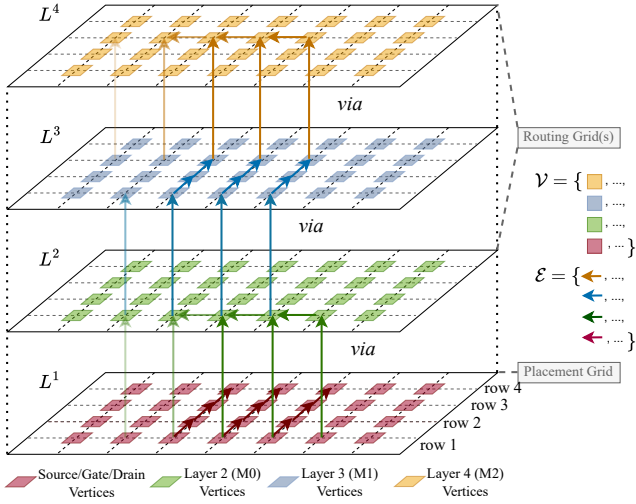


Fig. 6. An example of routing from both source/drain and gate locations in the placement grid to the frontside IO through L^2 , L^3 and L^4 . A super cut node, scx , is defined on each column on the placement grid to control the flow along the middle rows. On each routing grid, interconnections are made following the layer orientation. Between each pair of layers, vias are constructed at access points (colored squares) to make connections.

cut at odd columns—which enforces electrical isolation and requires terminals to be routed individually by metal layers. Conversely, $scx_c = 0$ implies a continuous active region where terminals are electrically shorted. The local connectivity allows the router to bypass flow requirements for individual terminals, provided the column itself is connected. scx_c is defined as an abstract cut value associated with column c .

For gate cuts, the minimum *cut width* is a design rule constraint specified in units of contacted poly pitch (CPP) [11]. We enforce this rule by grouping super cut nodes across adjacent even columns, as illustrated in Figure 7. For example, when the minimum cut width is two CPP, we enforce paired activation of scx_c on neighboring even columns. Different cut length settings may result in different cell widths: Figure 7(a) uses a 2-CPP cut and produces a layout with one fewer CPP compared to Figure 7(b), which uses a 1-CPP cut. Unless otherwise specified, we adopt a 2-CPP cut width, as it reduces the cell area of cross-coupled structures commonly found in D flip-flops, latches and multiplexers.

Flow Conservation Constraints. For each terminal $t_{n,k}$ of net n that is not merged by MOL routing, the flow must satisfy the following conservation laws:

$$\sum_{a \in \mathcal{A}^+(v)} f_{n,k}(a) - \sum_{a \in \mathcal{A}^-(v)} f_{n,k}(a) = \begin{cases} 1 & \text{if } v = s_n \\ -1 & \text{if } v = t_{n,k} \\ 0 & \text{otherwise} \end{cases} \quad (8)$$

C. Layer-based Fine-grained Design Rule Checking

CPCell enforces the complete set of conditional design rules specified by the target PDK [9], including Minimum Area Rule (MAR), Via Separation, End-Of-Line spacing (EOL), Step Height Rule (SHR) and Parallel Run Length (PRL). We parameterize these rules per layer and encode them using geometric variables to ensure full compliance.

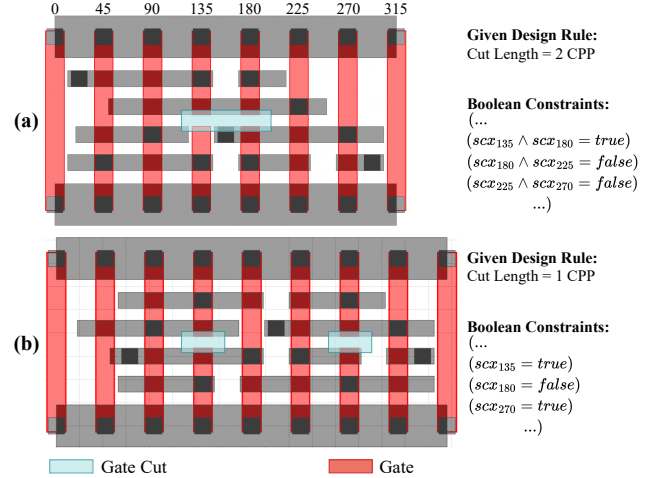


Fig. 7. An example on MUX2_X1 with different minimum cut width setting (1-CPP or 2-CPP). Cut width and cut shape are abstracted by super cut nodes scx . (a) When 2-CPP cut width is enforced, scx are grouped with adjacent columns to produce a longer cut shape. (b) When 1-CPP cut width is enforced, scx can be set to *True* individually to produce a shorter cut shape.

Geometric variables are introduced in [20] to indicate the End-Of-Line of a metal segment. We define geomet-

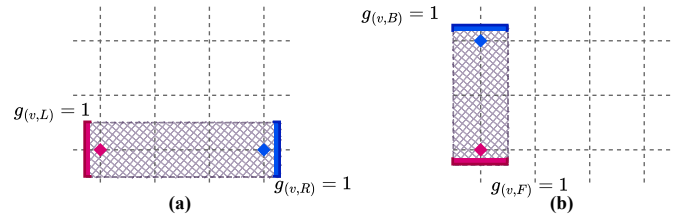


Fig. 8. An example of geometric variables defined on vertices. Each vertex is paired with a set of geometric variables corresponding to four directions: left, right (see (a)), front and back (see (b)), indicating the end of a metal segment.

ric variables (GVs) in our relative layered grid graph by assigning a set of Boolean variables to each vertex v : $g(v,L), g(v,R), g(v,F), g(v,B)$, representing the four directions—left, right, front and back.² On horizontal layers, a left-end GV $g(v,L)$ must be paired with exactly one right-end GV $g(u,R)$ to create a horizontal metal segment (see Figure 8(a)). Similarly, on vertical layers, a front-end GV $g(v,F)$ must be paired with one back-end GV $g(u,B)$ to create a vertical metal segment (see Figure 8(b)).

The non-uniformity in a relative layered grid graph requires the design rule parameters to be defined in terms of Euclidean distance. Prior methods [18] [20] [24] define these design rule parameters in terms of “number of vertices”, which is valid only in a uniform grid where all edge lengths are equal.

We input design rule parameters based on distance and track the total distance traveled along each path until the desired distance is attained. Design rule parameters can also be defined for each layer, as different layers may have varying metal pitches. Figure 9 demonstrates three of the design rules: MAR, Via Separation and EOL. Figure 9(a) shows the usage of geometric variables to encode the minimum area of a metal segment. Once $g(v_{2,R})$ is instantiated, the leftward

²Front corresponds to the bottom endpoint (lower row index) and Back corresponds to the top endpoint (higher row index).

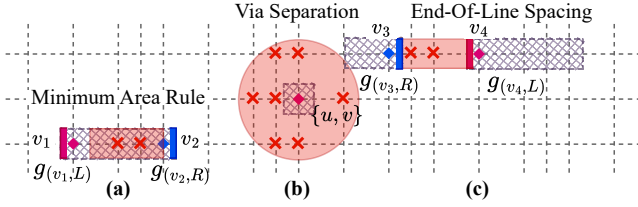


Fig. 9. Design rule checking on L^2 with distance input. The red-shaded region represents the prohibited area. (a) Minimum Area Rule (MAR) uses geometric variables and prohibits the current metal segments from ending too closely together. (b) Via Separation uses edge variables and prohibits any adjacent via within the Euclidean distance. (c) End-Of-Line spacing (EOL) uses geometric variables and prohibits any adjacent metal from ending too close to the current segment.

$g(v_{1,L})$ within the user-defined length is prohibited (indicated by the red cross sign). Similarly, Figure 9(c) shows the usage of geometric variables to encode the end-of-line spacing of a metal segment. Once $g(v_{4,L})$ is instantiated, the leftward $g(v_{3,R})$ within the user-defined length is prohibited (indicated by the red cross sign). Via Separation, on the other hand, does not use any geometric variables as illustrated in Figure 9(b). Each via is represented by an undirected edge $\{u, v\}$, where $u = (i - 1; r; c)$ and $v = (i; r; c)$. Once a via edge $\{u, v\}$ is instantiated, all vias within the user-defined radius are prohibited (indicated by the red cross sign). We encode these three rules using the Boolean cardinality constraint at-most-1 from CP-SAT. For other design rules, we examine all routing edges and their neighboring vertices to prohibit access within the specified distance.

III. MULTI-OBJECTIVES OPTIMIZATION

We formulate cell layout generation as a weighted multi-objective optimization problem solved using CP-SAT [39]. Prior methods [6] [20] apply lexicographic optimization, which minimizes objectives sequentially and may sacrifice optimality beyond the first few objectives. In contrast, we guarantee global optimality for the weighted-sum objective. While cell width and wirelength are sufficient to optimize primary cell-level metrics, *auxiliary objectives* play a critical role in steering the solver toward the optimal solution more efficiently. The complete set of objectives is defined as follows.

- (1) CW : Cell width measured in the number of contacted poly pitch (#CPP).
- (2) SGD : Total #source/gate/drain shared.
- (3) WL : Weighted wirelength.
- (4) DBX : Diffusion break placement, measured by the sum of placement column indices of all diffusion breaks.
- (5) $M2$: Top metal (M2) utilization, defined as the count of M2 tracks containing at least one active routing segment.

Together, the final objective function is:

$$\min \lambda_0 \cdot CW + \lambda_1 \cdot WL - \lambda_2 \cdot SGD - \lambda_3 \cdot DBX + \lambda_4 \cdot M2. \quad (9)$$

Unless stated otherwise, we use fixed integer weights in all experiments: $\lambda_0 = 1000$ and $\lambda_1 = \lambda_2 = \lambda_3 = \lambda_4 = 1$. We choose λ_0 to make CW the primary optimization target. SGD , DBX and $M2$ are auxiliary objectives that bias the search

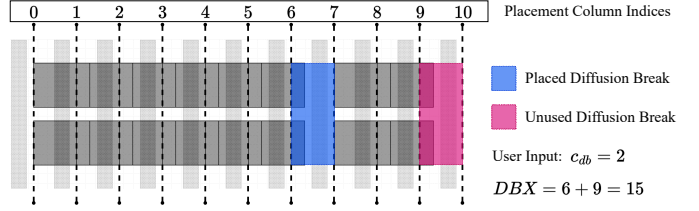


Fig. 10. Illustration of diffusion break placement and the DBX objective. When the maximum allowable diffusion breaks (c_{db}) exceed the layout requirements, the objective forces surplus breaks (pink) to the far right edge, minimizing the active cell width.

towards favorable structural patterns—such as increased MOL routing, rightward diffusion break placement and reduced M2 usage—thereby accelerating convergence without altering the optimal CW and WL . The runtime impact of each auxiliary objective is detailed in Section VI-B via an ablation study.

While the roles of SGD and $M2$ are relatively intuitive, the purpose of DBX is less obvious. Figure 10 shows an example of diffusion break placement and the DBX objective value. The DBX objective encourages diffusion breaks to be placed toward the right boundary of the layout canvas. Importantly, the user-defined parameter c_{db} serves only as an *upper bound* on the available diffusion breaks; CPCell automatically determines the actual number required for a layout. To ensure satisfiability, c_{db} is often set higher than the minimum necessary count. In these cases, the DBX objective naturally pushes any surplus (unused) diffusion breaks to the far right edge, preventing them from fragmenting the active region or increasing the effective cell width. Consequently, maximizing the rightward placement of diffusion breaks implicitly minimizes the occupied layout area, reinforcing the primary cell width objective.

IV. M0 PIN ENHANCEMENT

With enabled MOL routing, many nets no longer require M1 for internal routing, allowing M1 pins to be replaced by M0 pins and thereby increasing the number of access points available to the block-level router (see Figure 11). Within the given cell width, an M1 pin is accessible through four M2 routing tracks, an M0 pin can overlap up to seven M1 routing tracks, and it further benefits from additional routing resources enabled by non-1:1 gear ratios at the M1 layer. However, M0 pin accessibility is limited by routing blockages at both the M0 and M1 layers: pin-to-pin and pin-to-metal spacing rules limit extensibility at M0, while internal M1 metals may fully block routing tracks above. In CPCell, these effects are captured through two hard constraints—pin separation (PS) and minimum pin opening (MPO)—which together guarantee robust pin accessibility.

A. Pin Separation (PS)

Let \mathcal{P} denote the set of external pins. With M0 pin enablement, each pin $p \in \mathcal{P}$ is assigned at least one access vertex on the M0 layer. We denote the representative access vertex of pin p by

$$v_p = (2; r_p; c_p) \in V^2. \quad (10)$$

If the number of available M0 rows is at least $|\mathcal{P}|$, CPCell enforces PS as a hard constraint by requiring each pin to occupy a distinct M0 row:

$$r_{p_i} \neq r_{p_j}, \quad \forall p_i \neq p_j, p_i, p_j \in \mathcal{P}. \quad (11)$$

By prohibiting multiple pins from sharing the same M0 row, PS ensures spatial isolation among pin access points and complements the minimum pin opening constraint, which expands access regions along the M0 layer.

B. Minimum Pin Opening (MPO)

While PS enforces spatial isolation among pins, each external pin must also expose a sufficient number of access points to adjacent M1 routing tracks to ensure block-level routability. Minimum Pin Opening (MPO) enforces a hard lower bound on the horizontal extent of each M0 pin, measured by the number of accessible M1 routing tracks it overlaps.

For each external pin $p \in \mathcal{P}$, let $\mathcal{C}_p \subseteq \mathcal{C}^2$ denote the set of unoccupied and overlapped M1 routing tracks. The cardinality $|\mathcal{C}_p|$ therefore represents the number of M1 routing tracks covered by pin p . CPCell enforces the hard constraint:

$$|\mathcal{C}_p| \geq \Theta, \quad \forall p \in \mathcal{P}, \quad (12)$$

where Θ is a user-specified minimum pin opening parameter. This constraint ensures that each external pin exposes multiple access points to the block-level router, even in the presence of internal M1 routing blockages. Together with PS, MPO guarantees that pins are both spatially isolated and sufficiently exposed, providing a robust foundation for downstream routing under congested conditions.

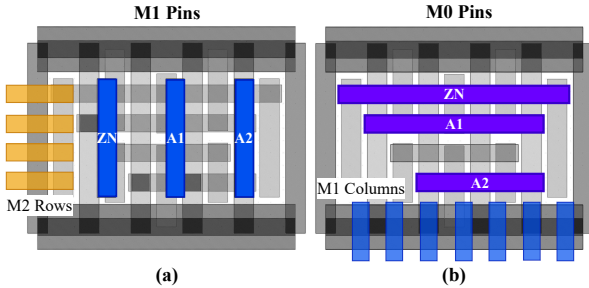


Fig. 11. Comparison of pin access for a NAND2_X2 cell under 3:2 GR: (a) M1 pins accessed by M2 routing rows (highlighted in golden yellow) and (b) M0 pins accessed by M1 routing tracks (highlighted in dark blue).

V. ACCELERATION TECHNIQUES

With gear ratio and offset enabled, the additional routing resource introduces more complexity as mentioned in [6]. SP&R uses partitioning that relies on expert knowledge of optimal datapath structures [19]. SMTCell-GR’s pre-partitioning [6] approach depends on solution reuse across related netlists. SO3 [5] relies on structural partitioning, misaligned gate specification and maximum occupying track. While effective in constrained settings, these approaches require manual intervention or prior design knowledge, limiting the scalability and generality when generating layouts for previously unseen netlists. To systematically address these challenges, we introduce a set of complementary acceleration techniques. First,

Algorithm 3: Graph Construction and Clustering

```

1 Input: Netlist, cluster bounds  $[k_{\min}, k_{\max}]$ 
2 Output: set of transistor clusters  $\mathit{C}lst$ 
3  $M \leftarrow \text{BUILD}\text{CIRCUIT}\text{GRAPH}(\text{Netlist});$ 
4  $M \leftarrow M \setminus \{\text{VDD}, \text{VSS}\}$ 
5 foreach net node  $n \in M$  such that  $\text{deg}(n) \leq 2$  do
6    $\{tr_i, tr_j\} \leftarrow \text{NEIGHBORS}(M, n);$ 
7    $\text{ADDEDGE}(M, tr_i, tr_j);$ 
8    $M \leftarrow M \setminus \{n\};$ 
9 for net node  $n \in M$  do
10  for neighbor  $tr \in \text{NEIGHBORS}(M, n)$  do
11     $w(n, tr) \leftarrow \text{deg}(n)$ 
12  $\mathbb{X} \leftarrow \text{KAMADA}\text{KAWAI}\text{LAYOUT}(M, w)$ 
13  $\mathit{C}lst, \text{noise} \leftarrow \text{HDBSCAN}(M, \mathbb{X}, k_{\min}, k_{\max});$ 
14 return  $\mathit{C}lst;$ 

```

transistor clustering exploits structural regularities in standard-cell netlists by grouping strongly coupled transistors, thereby reducing the effective placement granularity and search space. Second, *identical transistor partitioning* (ITP) reduces redundancy by enforcing a canonical ordering among electrically equivalent transistors. Third, *routing lower bound tightening* (RLBT) accelerates optimality certification by tightening the lower bound early in the search, reducing the time spent verifying optimality after a placement is found. Finally, for large-scale netlists where full certification becomes prohibitively expensive, *early termination* based on a relative gap provides a principled trade-off between runtime and optimality.

A. Transistor Clustering

We cluster transistors whose diffusion should be shared and impose structural constraints. Our approach is designed as a lightweight add-on to constraint solving. Figure 12 shows a one-to-one correspondence between the clusters from our method and the clusters in the optimal ground-truth layout of DFFHQX_X1. By utilizing these clusters to constrain the search space, the solver operates at the cluster-level rather than on individual transistors. Our clustering procedures are detailed in Algorithm 3 and summarized below:

Lines 1–8: We build a graph M with both transistors and nets represented as vertices. Connections are established exclusively between transistor vertices and net vertices: a link exists between a transistor tr and a net n if the net is incident to the transistor’s source, drain, or gate. We remove power and ground net nodes. We then remove any net node with degree ≤ 2 , and reconnect the incident transistors directly. This representation directly correlates with the potential candidate clusters for diffusion sharing and placement proximity.

Lines 9–12: We assign weights to fan-out edges from each net node proportional to the net degree and compute a two-dimensional embedding using the Kamada-Kawai spring model [17]. The model optimizes a spring-based energy function to preserve graph distances in Euclidean space, producing a layout in which strongly connected transistors are placed in close proximity.

Line 13–14: We apply Hierarchical Density-Based Spatial Clustering of Applications with Noise (HDBSCAN) [2] [26] to the embedded nodes, using the pairwise Euclidean distances in the embedding space as the clustering metric. HDBSCAN is chosen because it identifies density-based clusters without

requiring a predefined cluster count, and explicitly models a noise set. Transistors classified as *noise* are isolated or weakly connected in the embedding space and are treated as free-floating to preserve satisfiability. HDBSCAN also accepts minimum and maximum cluster sizes, denoted as k_{min} and k_{max} . k_{min} is always set to two as it is the minimum effective cluster size. k_{max} can range from two to six, depending on the netlist. When $k_{max} = 6$, the search space is aggressively pruned, but the solver may produce suboptimal solutions or even become unsatisfiable. Setting $k_{max} = 2$ is safer but produces limited speedup. The effect of these parameters is studied in Section VI-D. HDBSCAN returns a noise set of transistors and a set of density-based clusters $\{Clst_1, Clst_2, \dots\}$, where each cluster $Clst_k$ captures a group of transistors with strongly coupled connectivity. The noise set is discarded as it may over-constrain the layout and result in an unsatisfiable search space.

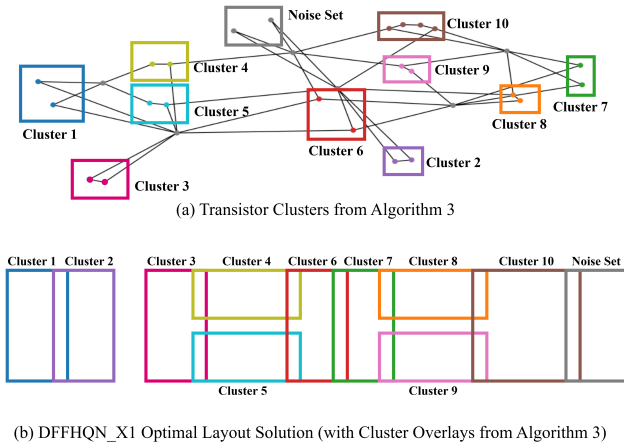


Fig. 12. Algorithm 3 reveals transistor clusters found in the optimal layout solution for DFFHQX1. (a) Identified 10 transistor clusters and one noise set via Algorithm 3. (b) The optimal layout solution generated without cluster-based constraints. The colored overlays show the correspondence between the clusters identified by Algorithm 3 and the clusters in the optimal placement.

Once transistor clusters are identified, we enforce diffusion continuity within each cluster. Let $Clst_k$ be a cluster comprising a set of transistors \mathcal{T}_k . For each transistor $tr \in \mathcal{T}_k$, let x_{tr} denote its left coordinate and w_{tr} its diffusion width. We enforce contiguous placement by constraining the total span of the cluster to equal the sum of the individual transistor width:

$$\left(\max_{tr \in \mathcal{T}_k} (x_{tr} + w_{tr}) \right) - \min_{tr \in \mathcal{T}_k} x_{tr} = \sum_{tr \in \mathcal{T}_k} w_{tr}. \quad (13)$$

The term $\max(x_{tr} + w_{tr}) - \min(x_{tr})$ represents the width of the bounding box of $Clst_k$. Enforcing equality with the sum of widths eliminates spacing gaps and overlaps, ensuring a single uninterrupted diffusion chain. For clusters containing both PMOS and NMOS devices, the total width $\sum w_{tr}$ is determined by the transistor type with the maximum aggregate diffusion width; transistors of the complementary type are constrained to lie within this spatial bound.

B. Identical Transistor Partitioning (ITP)

High-drive-strength cells (e.g., X2, X4 and X8 variants) contain groups of electrically identical transistors to achieve the target drive strength. Without additional partitioning, the solver must explore every permutation of these identical tran-

sistors, even though many such permutations yield identical layouts. CPCell partitions identical transistors into a canonical ordering. Given a set S of transistors with identical gate, source, drain and type attributes, we enforce ordering constraints of the form:

$$x_{tr_1} \leq x_{tr_2} \leq \dots \leq x_{tr_{|S|}}, \quad (14)$$

where x_{tr} denotes the placement coordinate. This symmetry breaking explores only one layout per permutation class.

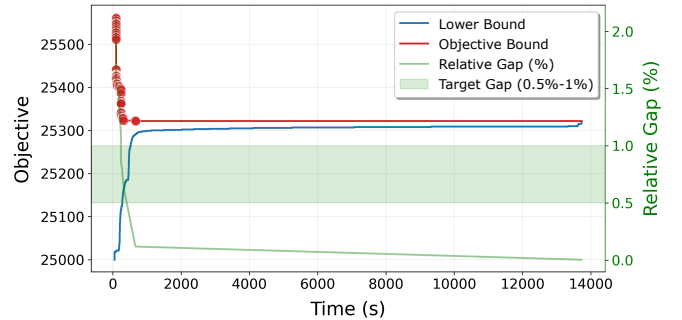


Fig. 13. Search progress of the CP-SAT solver for DFFHQX1 with cell-width (CW) and wirelength (WL) objectives. The red line graph denotes the objective, where each marker corresponds to the discovery of a new feasible layout, while the blue line graph represents the lower bound.

C. Routing Lower Bound Tightening (RLBT)

Based on the intermediate feasible placement solution, the half-perimeter wirelength (HPWL) [29] can be leveraged to derive a tight routing lower bound, significantly reducing the time required for optimality verification. The CP-SAT solver follows a classical branch-and-bound framework, augmented with linear programming (LP) relaxations and Boolean satisfiability (SAT) reasoning [27]. As shown in Figure 13, the solver maintains a red objective bound, given by the best intermediate feasible solution found so far, and a blue lower bound, derived from problem relaxations that certify no solution can achieve a lower objective bound. The search progressively tightens these bounds through branching, constraint propagation and relaxation refinement. Optimality is established when the objective and lower bounds converge.

Empirically, we observe that CP-SAT often identifies an optimal or near-optimal solution early in the search, whereas a substantial portion of the remaining runtime is devoted to tightening the lower bound to certify optimality. If the lower bound can be explicitly derived early on, we can reduce the runtime for such a certification. At block-level, HPWL is commonly used as a proxy for placement quality. At cell-level, we can use HPWL to estimate the wirelength of each net from the intermediate feasible placement solution, which serves as a routing lower bound. Once CP-SAT converges on a placement, this estimation immediately strengthens the lower bound, thereby accelerating optimality verification.

D. Early Termination & Relative Gap

To reduce solver runtime for large problem instances, we adopt an early-termination criterion based on the *relative gap* between the current objective bound and the lower bound. In

our experiments, the relative gap is set to 0.5% or 1% for large netlists and is defined as

$$\text{Relative Gap} = \frac{|\text{ObjectiveBound} - \text{LowerBound}|}{|\text{ObjectiveBound}|}. \quad (15)$$

From Figure 13, we observe that after the initial rapid objective improvement before 672 s, no better solution was found; instead, the solver devotes 13,062 s exclusively to tightening the lower bound to formally certify optimality. This behavior motivates the use of the relative gap for early termination. When the relative gap is used, we only guarantee optimality for the primary objective, cell width.

VI. CELL-LEVEL EXPERIMENTS ON GEAR-RATIO-ENABLED CELL LAYOUTS

Cell-level experiments were conducted on an Intel Core i9-12900K CPU with 64 GB of RAM using the Google OR-Tools CP-SAT solver (v9.14) [39] with six parallel search workers. All experiments target the 2-Fin 4-Routing Track (2F4T) configuration, which offers more constrained horizontal routing resources than the previously studied 3-Fin 5-Routing Track (3F5T) configuration [6], thereby more clearly exposing the impact of gear ratio selection on routing behavior. All results are generated using single diffusion break setting, which permits smaller spacing between adjacent transistors, thereby reducing cell width. We first analyze representative cells across different gear ratios and offset parameters. We then conduct an ablation study to examine the effects of individual objective functions and their relative weightings using DFFHQX1. Finally, we demonstrate the effectiveness of the proposed acceleration techniques using different D flip-flop designs and a high-drive-strength buffer.

A. Cell Metrics

We present a sensitivity study on gear ratios in Table III. For conciseness, we report results for 22 representative cells out of the 40 cells [6] designed under 2F4T configuration. We evaluate three gear ratio (GR) settings—45:45 (1:1), 45:30 (3:2) and 45:27 (5:3)—along with their respective offset counterparts. For a given GR parameter, the number of valid offset choices is determined by the alignment between the poly grid (pitch mp^1) and the M1 grid (pitch mp^3). Specifically, admissible offsets are restricted to integer multiples of the greatest common divisor (gcd), or $\text{gcd}(mp^3, mp^1)$ within one M1 period. 1:1 GR admits no valid offset, whereas 3:2 GR has one valid offset of 15 nm ($3 \cdot 2^\dagger$), and 5:3 GR has two valid offsets of 9 nm and 18 nm ($5 \cdot 3^\ddagger$ and $5 \cdot 3^{\ddagger\ddagger}$).

Across all settings, 1:1 GR consistently achieves the shortest CP-SAT runtime due to its smaller routing search space. However, its limited routing resources result in the largest average cell width and wirelength. Among non-1:1 GR settings, 3:2 and 5:3 GR exhibit identical average CPP and comparable wirelength and M2 usage. The offset variant of the 3:2 GR incurs no penalty in cell width, but introduces a slight increase in wirelength. In contrast, the offset variant of the 5:3 GR achieves the lowest average cell width (7.09 CPP), saving one CPP for the MUX2_X1 design. Overall, the 5:3 GR attains the lowest average wirelength across the benchmark

set, due to increased vertical routing resources. Nevertheless, transitioning from the 3:2 GR to the 5:3 GR—including their offset variants—does not consistently yield further wirelength reduction. In many cases, the wirelength under 3:2 and 5:3 GR are identical or differ only marginally, suggesting a saturation effect once routing resources exceed a critical threshold.

B. Ablation Study on Objectives

To evaluate the effectiveness of the objectives, we conduct an ablation study for DFFHQX1 by selectively enabling auxiliary objectives and examining their impact on solver runtime. We perform comparison studies of five objective combinations to isolate the individual and combined effects of auxiliary objectives on solver convergence behavior:

- (a) $\lambda_0 \cdot CW + \lambda_1 \cdot WL$
- (b) $\lambda_0 \cdot CW + \lambda_1 \cdot WL - \lambda_2 \cdot SGD$
- (c) $\lambda_0 \cdot CW + \lambda_1 \cdot WL - \lambda_3 \cdot DBX$
- (d) $\lambda_0 \cdot CW + \lambda_1 \cdot WL + \lambda_4 \cdot M2$
- (e) $\lambda_0 \cdot CW + \lambda_1 \cdot WL - \lambda_2 \cdot SGD - \lambda_3 \cdot DBX + \lambda_4 \cdot M2$

Study (a) considers only cell width and wirelength minimization and serves as the baseline configuration. Studies (b), (c) and (d) individually activate source/gate/drain sharing, diffusion break columns and M2 usage, respectively, to isolate their effects on solver convergence. Study (e) enables all auxiliary objectives to evaluate their combined impact on accelerating solver convergence.

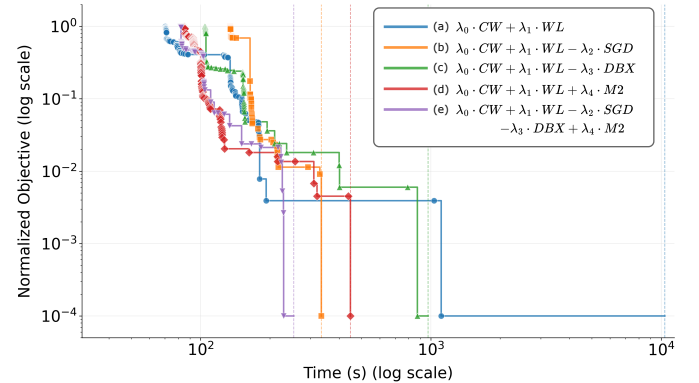


Fig. 14. Search progress of the CP-SAT solver for DFFHQX1 under different objective sets, shown on a logarithmic time scale with normalized objective values. The vertical dashed line marks the end of the search.

Figure 14 compares CP-SAT convergence for DFFHQX1 under different objective configurations. All configurations converge to the same final cell width and wirelength, confirming that auxiliary objectives do not affect layout optimality. However, convergence speed differs significantly. Enabling individual acceleration objectives substantially reduces runtime relative to the baseline: Study (b) achieves a 96.7% speedup, Study (c) achieves a 90.6% speedup and Study (d) achieves a 95.7% speedup. Finally, combining all auxiliary objectives in Study (e) yields the fastest convergence overall, achieving a 97.6% speedup. These results demonstrate that carefully designed auxiliary objectives can improve solver efficiency without degrading layout quality.

C. Effect of M0 Pin Accessibility Constraints

We model M0 pin accessibility using the count of unblocked on-grid access points, approximated by the number

TABLE III

CELL METRICS AND RUNTIMES FOR 2F4T GEAR-RATIO-ENABLED CELLS: 1:1 GR HAS NO OFFSET VARIANT; 3:2 GR HAS ONE 15 NM OFFSET (3:2[†]); AND 5:3 HAS TWO OFFSETS OF 9 NM AND 18 NM (5:3[†] AND 5:3^{††}), RESPECTIVELY. WIRELENGTH IS NORMALIZED TO THE 1:1 GR BASELINE.

Cell Name	#FET	#Net	Cell Width (CPP)					Normalized Wirelength					#M2					CP-SAT Runtime (s)								
			1:1	3:2	3:2 [†]	5:3	5:3 [†]	5:3 ^{††}	1:1	3:2	3:2 [†]	5:3	5:3 [†]	5:3 ^{††}	1:1	3:2	3:2 [†]	5:3	5:3 [†]	5:3 ^{††}						
AND2_X2	8	7	5	5	5	5	5	1.00	0.88	0.90	0.88	0.88	0.90	0	0	0	0	0	0	2	5	4	5	4	4	
AND3_X2	10	9	6	6	6	6	6	1.00	0.95	0.98	0.95	0.98	0.99	0	0	0	0	0	5	7	6	7	7	8		
AOI21_X1	6	8	5	4	4	4	4	1.00	0.77	0.80	0.77	0.80	0.77	0	0	0	0	0	2	2	2	3	3	3		
AOI22_X2	16	10	10	10	10	10	10	1.00	1.00	1.00	1.00	1.10	1.00	0	0	0	0	1	0	53	533	210	278	136	252	
BUF_X4	10	5	7	7	7	7	7	1.00	1.00	1.00	1.00	1.00	1.00	0	0	0	0	0	8	18	14	18	29	20		
BUF_X8	20	5	13	13	13	13	13	1.00	1.00	1.00	1.00	1.00	1.00	0	0	0	0	0	210	712	613	1105	2931	991		
DFFHQX_X1	24	17	14	14	14	14	14	1.00	1.00	1.02	1.00	1.00	1.01	2	2	2	2	2	121	254	300	352	429	414		
INV_X4	8	4	5	5	5	5	5	1.00	1.00	1.00	1.00	1.00	1.00	0	0	0	0	0	1	1	2	1	3	3		
INV_X8	16	4	9	9	9	9	9	1.00	1.00	1.00	1.00	1.00	1.00	0	0	0	0	0	1	1	2	3	3	3		
LHQ_X1	8	13	10	10	10	10	10	1.00	1.00	1.02	1.00	0.98	1.00	1	1	1	1	1	28	141	256	111	353	250		
MUX2_X1	12	12	8	8	8	8	7	7	1.00	0.93	1.01	0.93	0.89	0.94	1	1	1	1	1	9	9	13	26	9	9	
NAND2_X2	8	6	5	5	5	5	5	1.00	1.00	1.00	1.00	1.00	1.00	0	0	0	0	0	3	4	5	6	6	6		
NAND3_X2	12	7	7	7	7	7	7	1.00	1.00	1.00	1.00	1.00	1.00	1	1	1	1	1	12	24	28	45	51	50		
NAND4_X2	16	9	9	9	9	9	9	9	1.00	1.00	1.00	1.00	1.00	1.00	1	1	1	1	1	15	53	47	115	71	66	
NOR2_X2	12	8	5	5	5	5	5	1.00	1.00	1.00	1.00	1.00	1.00	0	0	0	0	0	3	5	5	6	6	6		
NOR3_X2	12	7	7	7	7	7	7	1.00	1.00	1.00	1.00	1.00	1.00	1	1	1	1	1	11	23	35	33	56	41		
NOR4_X2	16	9	9	9	9	9	9	9	1.00	1.00	1.00	1.00	1.00	1.00	1	1	1	1	1	19	61	58	122	97	123	
OAI21_X1	6	8	5	4	4	4	4	4	1.00	0.77	0.80	0.77	0.80	0.77	0	0	0	0	0	2	2	2	3	3	3	
OAI22_X2	16	10	10	10	10	10	10	10	1.00	1.00	1.00	1.00	1.10	1.00	0	0	0	1	0	48	456	167	297	73	266	
OR2_X2	8	7	5	5	5	5	5	1.00	0.85	0.86	0.84	0.83	0.87	0	0	0	0	0	3	5	4	5	5	4		
OR3_X2	10	9	6	6	6	6	6	6	1.00	0.96	0.98	0.95	0.98	0.99	0	0	0	0	0	5	9	7	11	8	8	
XOR2_X1	10	9	6	6	6	6	6	6	1.00	0.99	1.00	0.98	0.98	0.99	1	1	1	1	1	4	6	6	9	7	6	
Average			7.27	7.14	7.14	7.14	7.09	7.09	1.00	0.98	0.99	0.98	0.99	0.98	0.41	0.41	0.41	0.41	0.50	0.41	25.62	99.46	81.19	116.01	213.19	115.07

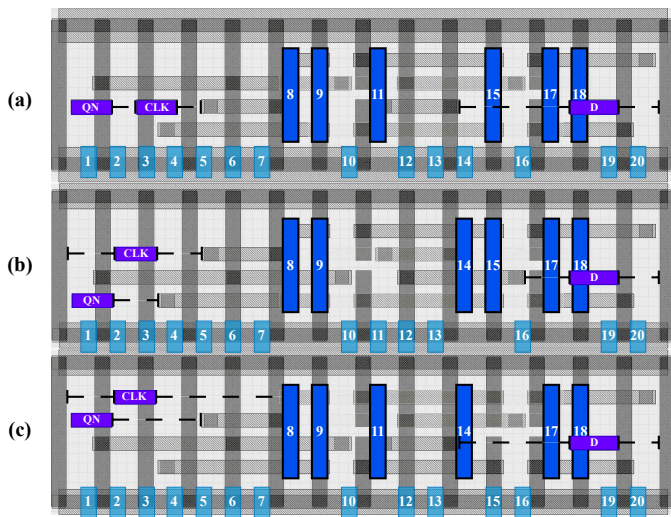


Fig. 15. Comparison of pin accessibility for DFFHQX_X1: (a) baseline, (b) PS enabled and (c) PS and MPO ($\Theta = 4$) enabled. M0 pins are shown in purple with dashed extensible regions; black-outlined M1 tracks indicate routing blockages and light-blue segments denote candidate access locations.

of M1 routing tracks that overlap each extended M0 pin. Prior works [16] [30] show that alignment to routing tracks and the resulting number of on-grid access points strongly correlate with pin accessibility, so the overlap count serves as a simple proxy. Figure 15 compares the DFFHQX_X1 layouts under progressively enabled pin accessibility constraints. We measure M0 pin accessibility by the number of unblocked M1 routing tracks that geometrically overlap each extended M0 pin. Table IV details the specific track counts and indices for each configuration. Figure 15(a) shows the baseline where pins share a single row, limiting track access. Figure 15(b) shows the effect of PS, which distributes pins across three rows and reduces interference. Figure 15(c) shows the highest accessibility achievable by combining PS with MPO ($\Theta = 4$). M0 pins extend to a minimum of four M1 access points, with the CLK pin reaching seven points.

TABLE IV

NUMBER AND INDICES OF M1 ROUTING TRACKS OVERLAPPING EACH EXTENDED M0 PIN FOR DFFHQX_X1 UNDER PS AND MPO (Θ).

	PS	MPO (Θ)	Pin	#Access	M1 Track Indices
(a)	–	–	QN	2	1, 2
			CLK	2	3, 4
			D	3	16, 19, 20
(b)	✓	–	QN	3	1, 2, 3
			CLK	4	1, 2, 3, 4
			D	2	19, 20
(c)	✓	4	QN	4	1, 2, 3, 4
			CLK	7	1, 2, 3, 4, 5, 6, 7
			D	4	15, 16, 19, 20

D. Effect of Acceleration Techniques

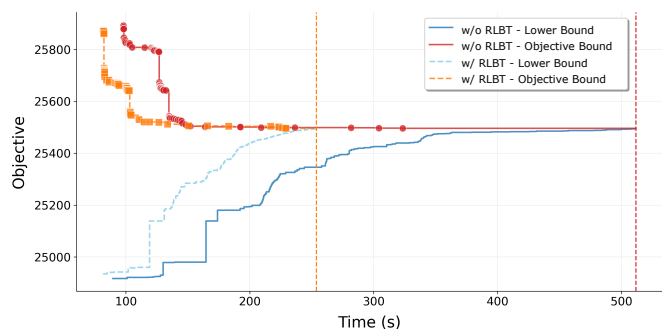


Fig. 16. CP-SAT search progress for DFFHQX_X1 with and without routing lower bound tightening, showing objective and lower bounds over time. The vertical dashed line marks search termination.

In this section, we evaluate the four acceleration techniques introduced in Section V. RLBT is always enabled in CPCell, as it directly reduces CP-SAT optimality certification overhead. As shown in Figure 13, a tight routing lower bound substantially accelerates search convergence, reducing solver runtime from 512 s to 254 s (50.4% speedup).

Table V details the runtime impact of acceleration techniques on cells sourced from PROBE3.0 [9] (DFFHQX_X1, DFFRNQ_X1), ASAP7 [32] (DFFHQX_X3/X4, BUF_X16), and SO3 [5] (2BDFHQX_X1) under 3:2 GR setting. A maximum runtime of 150000 s is imposed, after which the best feasible solution is reported. Transistor clustering consistently

improves runtime while preserving optimal width, wirelength, and M2 usage. Specifically, DFFHQX1 achieves a 36.6% speedup with clustering ($k_{\max} = 2$) and a 58.3% speedup (106 s) with clustering ($k_{\max} = 4$). Similarly, DFFRNQ_X1 achieves a 42.1% speedup with clustering ($k_{\max} = 2$); however, aggressive clustering ($k_{\max} = 4$) renders the run unsatisfiable. For high-drive-strength cells, combining clustering with ITP yields the highest gains. DFFHQX3 achieves a massive 88.9% speedup (9211 s to 1017 s) using ITP and clustering ($k_{\max} = 2$). DFFHQX4 achieves a 47.5% speedup using ITP and clustering ($k_{\max} = 3$), though larger cluster sizes again lead to unsatisfiability. For large-scale designs, early termination via relative gap is necessary to avoid timeouts. A 0.5% gap enables BUF_X16 to converge in 533 s with the optimal cell width. A 1.0% gap enables 2BDFHQX1 to converge in 15773 s with the optimal cell width. In summary, acceleration techniques significantly reduce search complexity but require careful tuning of cluster size and gap tolerance to maintain satisfiability.

TABLE V
CELL METRICS AND RUNTIME FOR 3:2 GR CELLS. CLST.: MAXIMUM CLUSTER SIZE k_{\max} . ITP: IDENTICAL TRANSISTOR PARTITIONING ENABLEMENT. GAP: RELATIVE GAP.

Cell Name	#FET	#Net	Acceleration			Width (CPP)	WL (nm)	#M2	RT (s)
			Clst.	ITP	Gap				
DFFHQX1	24	17	—	—	—	14	2541.0	2	254
			2	—	—	14	2541.0	2	161
			4	—	—	14	2541.0	2	106
DFFRNQ_X1	28	18	—	—	—	17	4166.0	4	11251
			2	—	—	17	4166.0	4	6512
			4	—	—	—	—	—	UNSAT
DFFHQX3	32	17	—	—	—	16	2826.5	2	9211
			2	✓	—	16	2826.5	2	1017
			3	✓	—	—	—	—	UNSAT
DFFHQX4	34	17	—	—	—	19	2966.5	2	133523
			3	✓	—	19	2966.5	2	70156
			4	✓	—	—	—	—	UNSAT
2BDFHQX1	44	29	—	—	—	25	5440.5	2	Timeout
			4	—	0.5%	25	5060.5	2	146785
			4	—	1.0%	25	6042.0	2	15773
BUF_X16	48	5	—	—	—	25	2876.0	0	Timeout
			—	✓	—	25	2017.5	0	Timeout
			—	✓	0.5%	25	2876.0	0	533

TABLE VI
CELL METRICS AND RUNTIME (RT) FOR DIFFERENT LAYOUT GENERATION TOOLS UNDER 3:2 GR AND 2F4T CONFIGURATION FOR D FLIP-FLOPS.

Cell Name	#FET	#Net	Tool	Width (CPP)	WL (nm)	#M2	RT (s)
DFFHQX1	24	17	SMTCell-GR [6]	18	4504.5	2	9075
			SO3 [5]	14	2577.0	2	262
			Our work	14	2541.0	2	106
			PROBE3.0 [9]	20	5550.0	5	4576
DFFRNQ_X1	28	18	SMTCell-GR [6]	—	—	—	Timeout
			SO3 [5]	17	4197.0	4	Timeout
			Our work	17	4166.0	4	6512
			PROBE3.0 [9]	—	—	—	Timeout
2BDFHQX1	44	29	SMTCell-GR [6]	—	—	—	Timeout
			SO3 [5]	—	—	—	Timeout
			Our work	25	6042.0	2	15773

E. Comparison with Other Tools for PROBE3.0

Table VI compares layout generation tools for D flip-flop designs using 3:2 GR against the best runtime results from Table V. All tools were tested on the same machine with a 150000 s timeout, using their respective acceleration techniques. Specifically, PROBE3.0 and SMTCell-GR use partitioned netlists from prior work [20] and the Z3 solver [34] with multi-threading. SO3 [5] uses Gurobi [37] with 12 work-

ers (double our CP-SAT configuration) and restricts topology optimization, gate alignments, diffusion breaks, and occupying track to reduce runtime. Given variations in rule support and encoding across tools, width serves as the primary metric, with wirelength and M2 track count provided for reference. CPCell requires no prior solution data, allowing seamless application to unseen netlists. It consistently achieves the smallest (or tied) cell width (CPP) with significantly lower runtime.

VII. BLOCK-LEVEL EVALUATIONS ON GEAR-RATIO-ENABLED CELL LAYOUTS

In this section, we explore example impacts of gear ratio at block-level. First, we confirm whether using offset cell layouts can in practice mitigate the placement legalization bottleneck. Second, we perform a comparative analysis of GR choices in terms of block-level PPA. Third, we evaluate IR-drop to show power integrity trade-offs introduced by GR alternatives.

These examples show how our framework can illuminate such phenomena as the following:

- (1) Offset cell layouts can improve the block PPA while also reducing runtime.
- (2) Although a smaller M1 pitch generally benefits block-level routing, it does not always lead to better PPA because of the trade-off between routing resources and wire capacitances.
- (3) A denser power distribution network (PDN) enabled by a GR with a smaller M1 pitch does not necessarily lead to smaller IR-drop compared to the sparser PDN of a GR with a larger M1 pitch.

Standard cell LVS and parasitic extraction are implemented with Cadence [36] Pegasus v21.3 and Quantus v21.1, and characterization is implemented with Cadence Liberate v21.1. Synthesis and place-and-route (P&R) are implemented with Synopsys [40] Design Compiler v20.09 and IC Compiler II v20.09, respectively. IR-drop is measured with Cadence Voltus v21.1. P&R and IR-drop are executed using 16 threads on a server equipped with an Intel Xeon Gold 6148 CPU (2.40 GHz, 80 threads) and 384 GB of memory. (Scripts are at [42].)

A. Gear Ratio & Offset Enablement

Previous study [6] of gear-ratio-enabled cells identifies a legalization failure at the block-level and suggests the addition of offset cells as a solution. In the following studies, we perform block-level P&R using 1:1, 3:2, and 5:3 GR cell layouts. To facilitate legalization in 3:2 GR 0-offset cells, cells with a 15 nm offset (denoted as 3:2[†]) are generated and grouped with 0-offset cells as an equivalent cell group (ECG).³ For 5:3 GR, 9 nm and 18 nm offset cells (5:3[†] and 5:3^{††}) are similarly grouped with 0-offset cells.

Table VII shows data for the JPEG Encoder [38] across target clock periods (TCPs) ranging from 100 ps to 400 ps. Performance is represented by the effective clock period (CKLP), which is obtained by subtracting the worst negative

³Equivalent Cell Groups are sets of functionally identical cells that have different physical variants, such as varying pin locations or colors. These groups allow EDA tools to perform variant-aware legalization, where a cell that does not align with a track can be swapped with a variant instead of being moved physically.

slack from the target clock period. Figure 17 shows the PPA comparison plot for 3:2 and 5:3 GR. For both gear ratios, adding offset variants reduces area with similar power and performance.

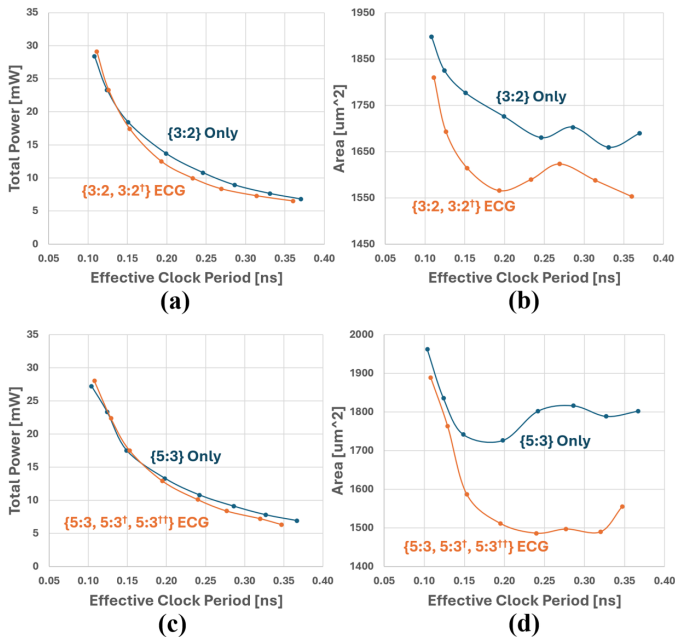


Fig. 17. Impact analysis results of offset cells on PPA. (a) 3:2 GR total power vs. effective CLKP; (b) 3:2 GR area vs. effective CLKP; (c) 5:3 GR total power vs. effective CLKP; (d) 5:3 GR area vs. effective CLKP.

Figure 18 shows P&R runtime comparison results. The runtime data confirm that ECGs yield shorter runtimes than 0-offset sets in most cases, possibly suggesting that finding legalizable physical variants takes less time than finding legalizable placement locations.

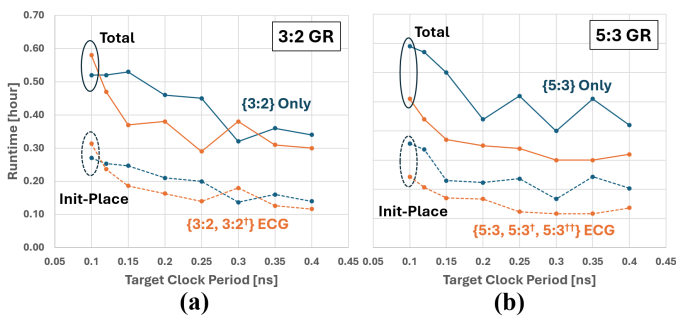


Fig. 18. Block-level P&R runtime comparison. (a) 3:2 GR; (b) 5:3 GR.

B. Choice of Optimal GR in DTCO Context

Although a smaller M1 pitch benefits block-level routing and reduces congestion, it also induces higher wire capacitance and increases power consumption. For this reason, a GR with a smaller M1 pitch does not guarantee the optimal choice in terms of PPA, and identifying the optimal GR can be a DTCO objective. Based on this belief, the PPA curves of each GR⁴ are compared in Figure 19, which shows that the 3:2 GR provides area benefits while maintaining power and performance levels equivalent to those of the 1:1 and 5:3 GRs.

⁴For the 3:2 and 5:3 GRs, ECGs are used.

- (1) Figure 19(a) indicates that power consumption is comparable across all GRs over the entire frequency range.
- (2) Figure 19(b) indicates that the 3:2 and 5:3 GRs provide significant area reduction compared to the 1:1 GR across the entire frequency range.
- (3) Figure 19(b) reveals a crossover in area efficiency: the 5:3 GR requires the least area at lower frequencies, whereas the 3:2 GR becomes more area-efficient in the high-frequency regime.

These studies suggest that selection of a best GR option may depend on the target design parameters.

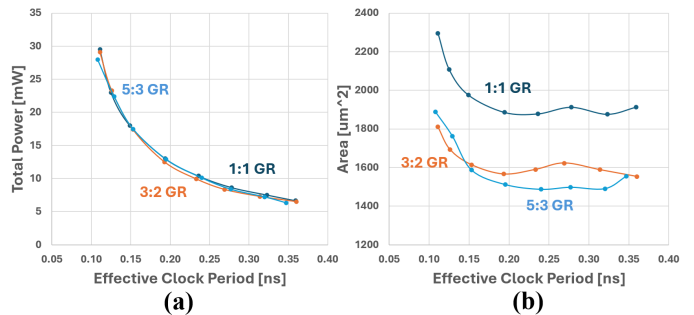


Fig. 19. PPA comparison for identifying the optimal GR in the DTCO context. (a) total power vs. effective clock period; (b) area vs. effective clock period.

C. Impact of Gear Ratio on IR-drop

Gear ratio is used not only for PPA benefit but also for IR-drop reduction. With a smaller M1 pitch, additional routing resources on M1 can be used to enable a finer PDN mesh to mitigate IR-drop. Figure 20(a) shows the setting of power stripe distance for each GR to 18 times the M1 pitch, which effectively places the worst IR-drop at approximately 10% of VDD at a clock period of 100 ps: 810 nm, 540 nm and 486 nm for the 1:1, 3:2 and 5:3 GR, respectively. Figure 20 also shows that the 3:2 GR has the worst IR-drop (77.0 mV), while the 1:1 GR has the lowest IR-drop (60.2 mV). The 3:2 and 5:3 GRs show a higher IR-drop than the 1:1 GR despite their denser PDNs, because their smaller areas induce higher current densities. From such IR-drop evaluation studies, a technology developer could, e.g., decide to apply the 5:3 GR to gain IR-drop benefits, accepting the higher cost required for denser M1 patterning. This highlights the necessity of holistic block-level evaluation in DTCO decision-making.

VIII. CONCLUSION

This paper extends prior studies on the impact of gear ratio on power, performance and area (PPA) with CPCell, a standard-cell layout generation framework that supports arbitrary gear ratios and offset variants for systematic DTCO exploration under the PROBE3.0 PDK. CPCell integrates acceleration techniques that preserve optimality in primary cell metrics while reducing CP-SAT runtime by up to 88.96%, enabling scalable generation for netlists with up to 48 transistors. Cell-level experiments demonstrate that non-1:1 gear ratios (3:2 and 5:3) reduce average cell width and wirelength relative to the 1:1 baseline by increasing vertical routing resources. In particular, the 5:3 gear ratio with offset achieves the smallest average cell width of 7.09 CPP. Block-level experiments confirm that gear-ratio-enabled cells achieve area and

TABLE VII
COMPARISON OF IMPLEMENTATION METRICS ACROSS TARGET CLOCK PERIODS

		Target Clock Period (ns)									
		0.10	0.12	0.15	0.20	0.25	0.30	0.35	0.40		
1:1 GR	#Insts	59472	46995	44790	43672	43215	43045	42815	42685		
	Wirelength (μm)	91637	83180	81885	72199	69993	66639	65531	65480		
	Total Power (mW)	29.5	23.0	18.0	13.0	10.4	8.7	7.5	6.7		
	Worst Negative Slack (ns)	-0.011	-0.005	0.001	0.006	0.014	0.022	0.027	0.041		
	Effective CLKP (ns)	0.111	0.125	0.149	0.194	0.236	0.278	0.323	0.359		
Area (μm^2)		2296	2108	1976	1886	1878	1912	1876	1912		
3:2 GR	0-offset Only	#Insts	57919	54403	52951	47918	46307	45677	45319	45253	
		Wirelength (μm)	73759	71986	71602	72681	65940	63185	63707	62488	
		Total Power (mW)	28.4	23.3	18.4	13.7	10.8	9.0	7.7	6.8	
		Worst Negative Slack (ns)	0.008	-0.004	-0.001	0.001	0.004	0.014	0.019	0.030	
		Effective CLKP (ns)	0.108	0.124	0.151	0.199	0.246	0.286	0.331	0.370	
	Mixed-offset	Area (μm^2)	1898	1826	1777	1726	1680	1703	1659	1690	
		#Insts	57429	44080	42490	41543	41216	41144	41112	41087	
		Wirelength (μm)	73338	77240	65216	59613	55371	54463	56735	55264	
		Total Power (mW)	29.1	23.3	17.4	12.5	10.0	8.4	7.3	6.5	
		Worst Negative Slack (ns)	-0.011	-0.006	-0.003	0.007	0.017	0.031	0.036	0.040	
Effective CLKP (ns)	0.111	0.126	0.153	0.193	0.233	0.269	0.314	0.360			
	Area (μm^2)	1810	1694	1614	1566	1590	1624	1588	1553		
	5:3 GR	0-offset Only	#Insts	59541	57871	52984	47065	54111	53054	52554	52623
			Wirelength (μm)	77526	81707	69595	73821	72639	69966	69677	68174
			Total Power (mW)	27.2	23.3	17.5	13.3	10.8	9.1	7.8	6.9
Worst Negative Slack (ns)			-0.004	-0.004	0.001	0.002	0.008	0.014	0.023	0.033	
Effective CLKP (ns)			0.104	0.124	0.149	0.198	0.242	0.286	0.327	0.367	
Mixed-offset		Area (μm^2)	1962	1836	1742	1726	1802	1816	1789	1802	
		#Insts	54311	50951	41213	39900	39594	38980	38808	38752	
		Wirelength (μm)	72570	69274	71586	66768	63838	56642	54316	55189	
		Total Power (mW)	28.0	22.4	17.5	12.9	10.1	8.4	7.2	6.3	
		Worst Negative Slack (ns)	-0.008	-0.009	-0.003	0.005	0.010	0.023	0.030	0.053	
Effective CLKP (ns)	0.108	0.129	0.153	0.195	0.240	0.277	0.320	0.347			
	Area (μm^2)	1888	1763	1586	1511	1486	1497	1490	1555		

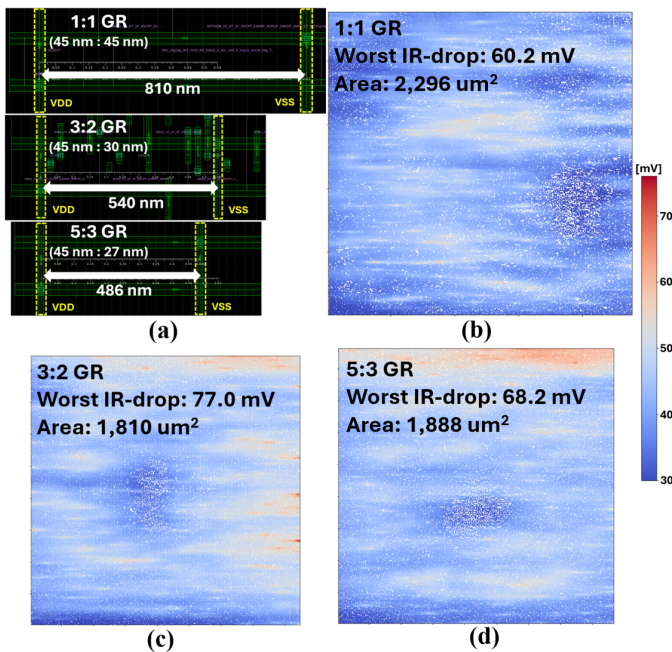


Fig. 20. Impact analysis results of offset cells on static IR-drop. Power stripe distances are adjusted according to the M1 pitch. (a) Power stripe distance for each GR; (b) IR-drop map of 1:1 GR; (c) IR-drop map of 3:2 GR; (d) IR-drop map of 5:3 GR.

wirelength reductions without degrading timing and power. While additional routing resources beyond a critical threshold yield diminishing returns, 3:2 and 5:3 gear ratios consistently outperform the 1:1 baseline in routability and layout efficiency, with 3:2 offering the best overall DTCO trade-off across

performance regimes. Overall, CCell provides a unified and extensible platform that bridges cell-level optimization and block-level implementation, enabling informed technology and architecture decisions for future technology nodes.

ACKNOWLEDGMENT

This work is partially supported by Logic Pathfinding Lab, Samsung Semiconductor Inc., NSF CCF-2110419, DARPA HR0011-18-2-0032, and the C-DEN center.

REFERENCES

- [1] K. Baek and T. Kim, "CSyn-fp: Standard Cell Synthesis of Advanced Nodes With Simultaneous Transistor Folding and Placement", *IEEE TCAD* 43(2) (2024), pp. 627-640.
- [2] R. J. G. B. Campello, D. Moulavi and J. Sander, "Density-Based Clustering Based on Hierarchical Density Estimates", *Proc. Pacific-Asia Conference on Knowledge Discovery and Data Mining*, 2013, pp. 160-172.
- [3] C.-K. Cheng, C.-T. Ho, D. Lee and B. Lin, "Monolithic 3D Semiconductor Footprint Scaling Exploration Based on VFET Standard Cell Layout Methodology, Design Flow, and EDA Platform", *IEEE Access* 10 (2022), pp. 65971-65981.
- [4] C.-K. Cheng, C.-T. Ho, D. Lee, B. Lin and D. Park, "Complementary-FET (CFET) Standard Cell Synthesis Framework for Design and System Technology Co-Optimization Using SMT", *IEEE Transactions on VLSI Systems* 29(6) (2021), pp. 1178-1191.
- [5] C.-K. Cheng, A. B. Kahng, B. Kang, S. Kang, J. Lee and B. Lin, "SO3-Cell: Standard Cell Layout Automation Framework for Simultaneous Optimization of Topology, Placement, and Routing", *Proc. ICCAD*, 2025, pp. 1-9.
- [6] C.-K. Cheng, A. B. Kahng, B. Lin, Y. Wang and D. Yoon, "Gear-Ratio-Aware Standard Cell Layout Framework for DTCO Exploration", *Proc. SLIP*, 2023, pp. 1-10.
- [7] C.-K. Cheng, B. Kang, B. Lin and Y. Wang, "Invited: Scaling Standard Cell Layout Using Track Height Compression and Design Technology Co-optimization", *Proc. ISPD*, 2025, pp. 11-19.

- [8] C. Chidambaram, A. B. Kahng, M. Kim, G. Nallapati, S. C. Song and M. Woo, "A Novel Framework for DTCO: Fast and Automatic Routability Assessment With Machine Learning for Sub-3nm Technology Options", *Proc. IEEE Symposium on VLSI Technology*, 2021, pp. 1–2.
- [9] S. Choi, J. Jung, A. B. Kahng, M. Kim, C.-H. Park, B. Pramanik and D. Yoon, "PROBE3.0: A Systematic Framework for Design-Technology Pathfinding With Improved Design Enablement", *IEEE TCAD* 43(4) (2024), pp. 1218-1231.
- [10] K. Han, A. B. Kahng and H. Lee, "Evaluation of BEOL Design Rule Impacts Using an Optimal ILP-Based Detailed Router", *Proc. DAC*, 2015, pp. 1-6.
- [11] K. Han, A. B. Kahng, H. Lee and L. Wang, "ILP-Based Co-Optimization of Cut Mask Layout, Dummy Fill, and Timing for Sub-14nm BEOL Technology", *Proc. SPIE Photomask Technology*, 2015, pp. 80-93.
- [12] C.-T. Ho, A. Ho, M. Fojtik, M. Kim, S. Wei, Y. Li, B. Khailany and H. Ren, "NVCell 2: Routability-Driven Standard Cell Layout in Advanced Nodes With Lattice Graph Routability Model", *Proc. ISPD*, 2023, pp. 44–52.
- [13] T. C. Hu, "Multi-Commodity Network Flows", *Operations Research* 11(6) (1963), pp. 844-858.
- [14] J. Jeong, S. Chung, K. Jo and T. Kim, "Synthesis and Utilization of Standard Cells Amenable to Gear Ratio of Gate-Metal Pitches for Improving Pin Accessibility", *Proc. DATE*, 2023, pp. 1–6.
- [15] A. B. Kahng, S. Kang, S. Kim, J. Lee and D. Yoon, "Au-MEDAL: Adaptable Grid Router with Metal Edge Detection and Layer Integration", *Proc. ASP-DAC*, 2026, to appear.
- [16] A. B. Kahng, J. Kuang, W.-H. Liu and B. Xu, "In-Route Pin Access-Driven Placement Refinement for Improved Detailed Routing Convergence", *IEEE TCAD* 41(3) (2022), pp. 784-788.
- [17] T. Kamada and S. Kawai, "An Algorithm for Drawing General Undirected Graphs", *Information Processing Letters* 31(1) (1989), pp. 7-15.
- [18] I. Kang, C. Han, D. Park and C.-K. Cheng, "Fast and Precise Routability Analysis With Conditional Design Rules", *Proc. SLIP*, 2018, pp. 1–8.
- [19] D. Lee, *Logical Reasoning Techniques for VLSI Applications*, Ph.D. dissertation, University of California, San Diego, 2022.
- [20] D. Lee, C.-T. Ho, I. H.-R. Jiang, B. Lin and C.-K. Cheng, "SP&R: Constraint-Programming-Based Simultaneous Place-and-Route for Standard Cell Synthesis of Advanced Nodes", *IEEE TCAD* 40(12) (2021), pp. 2541-2554.
- [21] L. Liebmann, V. Gerousis, P. Gutwin, X. Zhu and J. Petykiewicz, "Exploiting regularity: breakthroughs in sub-7nm place-and-route", *Proc. Design for Manufacturability through Design-Process Integration XI* 10148, SPIE, 2017.
- [22] S. Maheshwaram, S. K. Manhas, G. Kaushal, B. Anand and N. Singh, "Vertical Silicon Nanowire Gate-All-Around Field Effect Transistor Based Nanoscale CMOS", *IEEE Electron Device Letters* 32(8) (2011), pp. 1011-1013.
- [23] L. De Moura and N. Björner, "CP-SAT: An Efficient SMT Solver", *Proc. International Conference on Tools and Algorithms for the Construction and Analysis of Systems*, 2008, pp. 337–340.
- [24] D. Park, I. Kang, Y. Kim, S. Gao, B. Lin and C.-K. Cheng, "ROAD: Routability Analysis and Diagnosis Framework Based on SAT Techniques", *Proc. ISPD*, 2019, pp. 65–72.
- [25] E. Park and T. Song, "Complementary FET (CFET) Standard Cell Design for Low Parasitics and Its Impact on VLSI Prediction at 3 nm Process", *IEEE Transactions on VLSI Systems* 31(2) (2023), pp. 177-187.
- [26] F. Pedregosa et al., "Scikit-learn: Machine Learning in Python", *Journal of Machine Learning Research* 12 (2011), pp. 2825-2830.
- [27] L. Perron, F. Didier and S. Gay, "The CP-SAT-LP Solver", *Proc. International Conference on Principles and Practice of Constraint Programming*, 2023, pp. 3:1–3:2.
- [28] H. Ren, M. Fojtik and B. Khailany, "NVCell: Standard Cell Layout in Advanced Technology Nodes With Reinforcement Learning", *Proc. DAC*, 2021, pp. 1165–1170.
- [29] C. Sechen and A. Sangiovanni-Vincentelli, "The TimberWolf Placement and Routing Package", *IEEE Journal of Solid-State Circuits* 20(2) (1985), pp. 510-522.
- [30] F. Sun, H. Chen, C. Chen, C. Hsu and Y. Chang, "A Multithreaded Initial Detailed Routing Algorithm Considering Global Routing Guides", *Proc. ICCAD*, 2018, pp. 1-7.
- [31] S. M. Y. Sherazi et al., "Standard-Cell Design Architecture Options Below 5 nm Node: The Ultimate Scaling of FinFET and Nanosheet", *Proc. SPIE Design-Process-Technology Co-optimization for Manufacturability XIII* 10962 (2019), Art. no. 1096202.
- [32] V. Vashishtha, M. Vangala and L. T. Clark, "ASAP7 Predictive Design Kit Development and Cell Design Technology Co-optimization: Invited Paper", *Proc. ICCAD*, 2017, pp. 992–998.
- [33] X. Xu, B. Cline, G. Yeric, B. Yu and D. Z. Pan, "Self-Aligned Double Patterning Aware Pin Access and Standard Cell Layout Co-Optimization", *IEEE TCAD* 34(5) (2015), pp. 699-712.
- [34] C. Barrett, R. Sebastiani, S. A. Seshia and C. Tinelli, "Satisfiability Modulo Theories", *Handbook of Satisfiability*, Amsterdam, IOS Press, 2021, pp. 1267–1329.
- [35] IEEE International Roadmap for Devices and Systems (IRDS), 2022 [Online]. Available: <https://irds.ieee.org/irds2022>
- [36] Cadence Pegasus, Quantus and Voltus. <https://cadence.com>
- [37] Gurobi Optimization, LLC, *Gurobi Optimizer Reference Manual*, 2025. <https://www.gurobi.com>
- [38] OpenCores JPEG Encoder. <https://opencores.org/projects/mkjpeg>
- [39] L. Perron and V. Furnon, *OR-Tools*, Google Optimization Tools, 2025. <https://github.com/google/or-tools/releases/tag/v9.14>
- [40] Synopsys Design Compiler, IC Compiler II. <https://synopsys.com>
- [41] SMTCellUCSD: Cell Layout Generation for DTCO/STCO Exploration Toolkit. <https://github.com/ckchengusd/SMTCellUCSD>
- [42] CP-SAT based Standard Cell Layout Generator. <https://github.com/ABKGroup/CPCellUCSD>



Chung-Kuan Cheng is Distinguished Professor of CSE and Adjunct Professor of ECE at the University of California, San Diego. His research interests include machine learning and design automation for microelectronic circuits. He received the Ph.D. degree in Electrical Engineering and Computer Sciences from the University of California, Berkeley.



Andrew B. Kahng is Distinguished Professor of CSE and ECE at the University of California, San Diego. His interests include IC physical design, the design-manufacturing interface, combinatorial optimization, and AI/ML for EDA and IC design. He received the Ph.D. degree in Computer Science from the University of California, San Diego.



Bill Lin received BS, MS and PhD degrees in EECS from UC Berkeley. He is a Professor of Electrical and Computer Engineering at UC San Diego, affiliated with the Center for Wireless Communications and the Center for Networked Systems, CNS. He is also currently the Associate Dean for Research for the Jacobs School of Engineering. He has over 250 publications, multiple best-paper awards, six patents and extensive IEEE/ACM service.



Yucheng Wang is a Ph.D. student in the Computer Science Department of the University of California at San Diego. He received his bachelor's degree in Computer Science from Purdue University, West Lafayette, in 2021. His research interests include standard-cell layout automation, design technology co-optimization strategies and graph visualization.



Dooseok Yoon received the M.S. degree in electrical and computer engineering from the University of California at San Diego, La Jolla, CA, USA, in 2024. He is currently pursuing the Ph.D. degree at the University of California at San Diego, La Jolla. His research interests include VLSI physical design and design-technology co-optimization.